Multilayer Topology Optimization of Wideband SIW-to-Waveguide Transitions

Emadeldeen Hassan, Benedict Scheiner, *Student Member, IEEE*, Fabian Michler, *Student Member, IEEE*, Martin Berggren, Eddie Wadbro, Franz Röhrl, Stefan Zorn, Robert Weigel, *Fellow, IEEE*, and Fabian Lurz, *Member, IEEE*

***Abstract*— This article utilizes a topology optimization approach to design planar multilayer transitions between substrate integrated waveguides (SIWs) and rectangular waveguides (RWGs). The optimization problem is formulated based on the modal field analyses and Maxwell's equations in the time domain solved by the finite-difference time-domain (FDTD) method. We present a time-domain boundary condition based on the Klein–Gordon equation to split traveling waves at homogeneous waveguide ports. We employ the boundary condition to compute portal quantities and to devise an adjoint-field system that enabled an efficient computation of the objective function gradient. We solve design problems that include more than 105 000 design variables by using less than 400 solutions of Maxwell's equations. Moreover, a new formulation that effectively combats the development of in-band resonances in the design is presented. The transition configuration allows the direct mount of conventional RWG sections on the circuit board and aims to cover the entire K-band. The guiding structure of the optimized transition requires blind vias, which is realized by a simple and cost-efficient technique. In addition, the transition is optimized for three different setups that can be used to provide different field polarizations. The proposed transitions show less than 1-dB insertion loss and around 15-dB return loss over the frequency interval 18–28 GHz. Several prototypes are fabricated with an excellent match between the simulation and measurement results.**

***Index Terms*— Finite-difference time-domain (FDTD), Klein–Gordon equation, modal field analysis, multilayer transitions, planar circuits, substrate integrated waveguides (SIW), topology optimization, waveguides, wideband systems.**

Manuscript received August 28, 2019; revised November 25, 2019; accepted November 25, 2019. This work was supported in part by the Swedish strategic research program eSSENCE and in part by the FAU Visiting Professorship Program of the Bavarian State Ministry of Science, Research and the Arts. *(Corresponding author: Emadeldeen Hassan.)*

E. Hassan is with the Department of Computing Science, Umeå University, SE-901 87 Umeå, Sweden, and also with the Department of Electronics and Electrical Communications, Menoufia University, Menouf 32952, Egypt (e-mail: emad@cs.umu.se).

B. Scheiner, F. Michler, R. Weigel, and F. Lurz are with the Institute for Electronics Engineering, Friedrich-Alexander-Universitët Erlangen-Nürnberg, 91058 Erlangen, Germany.

M. Berggren and E. Wadbro are with the Department of Computing Science, Umeå University, SE-901 87 Umeå, Sweden.

F. Röhrl is with Rohde & Schwarz GmbH & Company, KG, 94244 Teisnach, Germany.

S. Zorn is with Rohde & Schwarz GmbH & Company, KG, 94244 Teisnach, Germany, and also with the Deggendorf Institute of Technology, 94469 Deggendorf, Germany.

Color versions of one or more of the figures in this article are available online at http://ieeexplore.ieee.org.

Digital Object Identifier 10.1109/TMTT.2019.2959759

I. Introduction

THE DESIGN of broadband radio frequency (RF) transitions is a common and yet still very elaborate task in modern microwave engineering. Typical applications that require a well-matched and low-loss transition, e.g., from a printed circuit board (PCB) to a waveguide or horn antenna, include broadband radar and wireless sensing systems [1]–[5]. Likewise, due to their excellent shielding, low-loss, and power handling properties of waveguides, these transitions are often used in high data communication [6], [7]. With emerging technologies such as cyber-physical systems and Internet of Space (IoS) with microsatellite and nanosatellite [8], [9], it can be expected that applications and requirements for high-performance transitions will continue to grow in the future.

Designing such transitions, however, still requires considerable human time and effort. The design process usually starts with a rough conceptual idea that is then parameterized with a few design variables and analyzed and adapted by a professional microwave engineer in the 3-D field simulations. Various such concepts to connect a PCB to a waveguide or horn antenna have already been published [10]–[17]. Nevertheless, these approaches demand either rather high manufacturing or assembling efforts [10]–[15] or are hardly suitable for broadband applications [16], [17]. Also, commercially available broadband transitions, which for example use coaxial probes as feeds in waveguides, have significant disadvantages due to high costs even at high volumes.

Waveguide ports are crucial elements in the analysis of waveguide-based devices. Two concepts are widely used to model waveguide ports in the time domain. The first is to use a modal field analysis to design the boundary conditions for waveguide problems [18]–[23]. Alimenti *et al.* [21] proposed a boundary condition based on a modal field analysis and a time-domain translation operator. Their boundary condition absorbs the outgoing modes and is capable to impose source signals. This concept was employed, for instance, to provide compact wideband equivalent models to analyze complex RF systems [24], [25]. The second concept to model waveguide ports is by combining the total-field scattered-field formulation and perfectly matched layers (PMLs). Recently, Chen *et al.* [26] proposed an inhomogeneous waveguide port for S-parameters extraction by the time-domain discontinuous Galerkin method. Their waveguide port combines the modal

field analysis to impose source signals and a PML to absorb the outgoing signals.

Topology optimization techniques have revolutionized the design process in various engineering disciplines [27]–[29]. One substantial benefit of employing such techniques is their ability to offer new conceptual designs. These techniques were initially proposed for structural optimization, and then, they have been successfully extended to various electromagnetic design problems (see [30]–[33] and the references therein). The high-dimensional parameterization offered by these techniques not only has the potential to reveal novel designs with outstanding performance but allows the inclusion of manufacturing constraints in the design phase as well [34]. In this way, novel designs, which would be difficult or impossible to imagine with manual design procedures, can be realized.

Recently, topology optimization has emerged as a promising approach to design microwave transitions [34]–[36]. Because of the dispersive nature of waveguides, the portal quantities used to formulate these optimization problems were treated based on two concepts. The first was to employ the total-field scattered-field approach combined with a PML, as an absorbing boundary condition, to excite the waveguides. The second concept was to include coaxial-to-waveguide transition sections in the model to circumvent dealing with dispersive waveguide ports. Besides, these design problems used only a single-layer PCB and were accordingly, for planar devices, very limited in bandwidth and matching. Since in the millimeter-wave regime and beyond, a single-layer substrate could be too delicate, it is common to utilize multilayer PCBs to mechanically stabilize the entire circuit board or to provide RF and dc routing lines [37].

In this article, we present a new topology optimization approach to design multilayer planar transitions that offer significantly more design freedoms. The transitions make use of three topology optimized copper layers of a low-cost four-layer RF stack-up. The approach employs the modal field analyses and solutions of Maxwell's equation in the time-domain by the finite-difference time-domain (FDTD) method. We employ the Klein–Gordon equation and introduce a time-domain boundary condition to split traveling waves at homogeneous waveguide ports. The proposed boundary condition models waveguide ports and makes it possible to derive an adjoint system that enabled efficient computations of the derivatives of the observed quantities with respect to the design variables. In addition, we propose a formulation that for the first time addresses in-band resonances and makes the optimized designs less prone to this issue. The treatment of the design problem in the time domain together with the novel portal problem formulation makes it highly efficient to optimize the waveguide transitions for wideband performance. The optimized transitions are suitable for cost-efficient mass production by conventional PCB processes. Moreover, the transitions are easy to mount to conventional rectangular waveguides (RWGs) without using any further components as stepped transformers or back cavities. Two configurations are presented, which can be utilized in a predefined fixture to provide dual polarization. Section II describes the problem setup. In Section III, we present our formulation of the design process as a topology optimization problem with comprehensive details on numerical treatments. Section IV presents the numerical and experimental results for transitions covering the entire K-band. The results are discussed and compared with some state-of-the-art transitions in Section VII, and the conclusion is given in Section VIII.

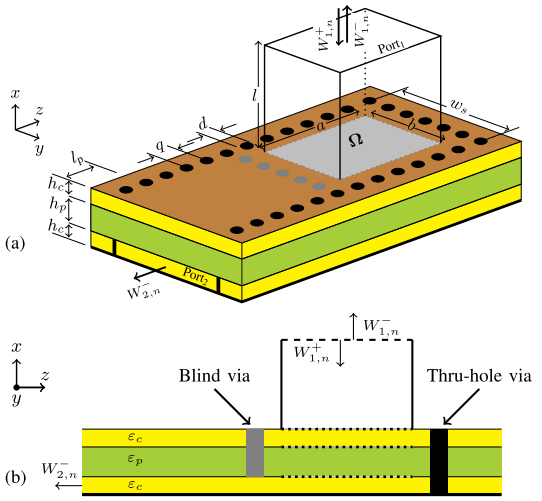

Fig. 1. (a) Geometry of the three-layer SIW-to-RWG transition. (b) Cross-sectional view through the xz plane showing a blind (gray) via, a thru-hole (black) via, and the three sheets (dotted lines) where the copper distribution will be optimized.

II. Conceptual Layout

Fig. 1 shows the conceptual geometry of the substrate integrated waveguide (SIW)-to-RWG-transition addressed in this article. The device consists of four sheets of copper embracing three dielectric substrates. The middle substrate (prepreg) has a thickness h_p and a dielectric permittivity ε_p, whereas both the top and bottom substrates (cores) have a thickness h_c and a permittivity ε_c. The first substrate from the bottom hosts an SIW, which we aim to match to an RWG mounted on top of the third substrate. The sidewalls of the SIW are formed using three rows of thru-hole metallic vias (colored black in the figure) that cross through the three substrates. To keep a signal path between the SIW and the RWG, a row of blind vias (colored gray in the figure) crosses through the top and middle substrates only, as shown in Fig. 1. Both the SIW and the RWG are assumed to be matched on the other side of the transition.

We aim to match the SIW to the RWG over the frequency band 18–28 GHz, which contains the entire K-band, by optimizing the copper distribution in the design domain Ω. The domain Ω comprises three planar sheets of copper with areas $a \times b$ per sheet, where a and b are the RWG inner dimensions. Two sheets are located between the prepreg and the two cores, and the third between the top core and free space. The locations of the three sheets are marked by the dotted lines in Fig. 1(b).

III. Computational Model

This section presents the computational model used for the optimization problem stated earlier. First, we review the governing equations and outline the derivation of some

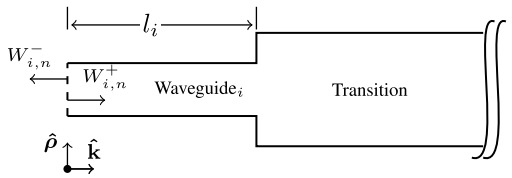

Fig. 2. Schematic diagram illustrating a waveguide section, at whose end signals are transmitted and received, connected to the transition domain; $i = 1$, 2 refers to the RWG and SIW, respectively.

time-domain portal quantities at the end of the RWG (Port_1) and the SIW (Port_2) (see Fig. 1). These are used for two purposes: 1) to set boundary conditions for the computations and 2) to define objective functions for the optimization. Second, we formulate an optimization problem based on these portal quantities as well as in-domain measures. Third, we present the numerical approach used to solve the governing equations and the optimization problem.

A. Portal Quantities

The time–space relationship between the electric field $\mathbf{E}$ and the magnetic field $\mathbf{H}$ is governed by Maxwell's equations

$$\partial_t \varepsilon \mathbf{E} + \sigma \mathbf{E} - \nabla \times \mathbf{H} = \mathbf{0} \tag{1a}$$

$$\partial_t \mu \mathbf{H} + \nabla \times \mathbf{E} = \mathbf{0} \tag{1b}$$

where ε, μ, and σ, are the medium's permittivity, permeability, and electric conductivity, respectively. The transition region subject to design is on each side surrounded by the waveguide sections. At the end of these sections, boundary conditions are applied in the form of an imposed incoming signal and absorbed outgoing signals. Thus, schematically, each of the waveguides is attached to the transition region as shown in Fig. 2, in which the energy influx of the in- and outgoing signals is denoted $W_{i,n}^+$ and $W_{i,n}^-$, respectively. (Index n refers to a mode number as outlined next.)

The derivation of the portal quantities will be based on modal expansions in the waveguides. Under the assumption of a lossless medium in a waveguide, the transversal electric $\mathbf{E}_\text{T}$ and magnetic $\mathbf{H}_\text{T}$ fields in the waveguides satisfy the expansions

$$\mathbf{E}_\text{T}(\mathbf{r}, t) = \sum_{n=1}^{\infty} V_n(k, t)\mathbf{e}_n(\boldsymbol{\rho}) \tag{2a}$$

$$\eta \mathbf{H}_\text{T}(\mathbf{r}, t) = \sum_{n=1}^{\infty} I_n(k, t)\mathbf{h}_n(\boldsymbol{\rho}) \tag{2b}$$

where $V_n(k, t)$ and $I_n(k, t)$ are modal voltages and currents, $\mathbf{e}_n(\boldsymbol{\rho})$ and $\mathbf{h}_n(\boldsymbol{\rho})$ are the corresponding orthonormal modal bases of the electric and magnetic fields, and $\eta = \sqrt{\mu/\varepsilon}$. Here, the position vector $\mathbf{r}$ is split in the transverse and longitudinal directions

$$\mathbf{r} = \boldsymbol{\rho} + k\hat{\mathbf{k}} \tag{3}$$

where $\boldsymbol{\rho}$ is a position vector in the cross section and $\hat{\mathbf{k}}$ is the waveguide direction of propagation shown in Fig. 2. The modal bases $\mathbf{e}_n$ and $\mathbf{h}_n$ depend on the waveguide cross section and are computed by solving two eigenvalue problems that result in orthonormal bases for the TE and TM modes [19], [38], with $\mathbf{h}_n = \hat{\mathbf{k}} \times \mathbf{e}_n$. The waveguides are here rectangular and filled with a nondispersive dielectric, which means that the eigenfunctions are given by simple formulas involving tensor products of trigonometric functions [39]. For inhomogeneously filled waveguides and more general cross-sectional shapes, modal bases can be computed using numerical methods [26].

The orthonormality of the modal bases—that is

$$\int_\text{S} \mathbf{e}_m(\boldsymbol{\rho}) \cdot \mathbf{e}_n(\boldsymbol{\rho}) d\text{S} = \int_\text{S} \mathbf{h}_m(\boldsymbol{\rho}) \cdot \mathbf{h}_n(\boldsymbol{\rho}) d\text{S} = \delta_{mn} \tag{4}$$

in which S is the cross section, and where δ_{mn} is Kronecker delta—means that

$$V_n(k, t) = \int_\text{S} \mathbf{E}_\text{T}(\mathbf{r}, t) \cdot \mathbf{e}_n(\boldsymbol{\rho}) d\text{S} \tag{5a}$$

$$I_n(k, t) = \int_\text{S} \eta \mathbf{H}_\text{T}(\mathbf{r}, t) \cdot \mathbf{h}_n(\boldsymbol{\rho}) d\text{S}. \tag{5b}$$

Kristensson [38] shows that both the modal voltages and currents satisfy the 1-D Klein–Gordon equation

$$\partial_t^2 f_n + \lambda_n^2 \, c^2 \, f_n - c^2 \partial_k^2 f_n = 0 \tag{6}$$

where $c = \sqrt{\mu/\varepsilon}$ is the phase velocity and λ_n is the nth eigenvalue, as well as the equations

$$\partial_t I_n + c\partial_k V_n = 0, \quad \text{for TE modes} \tag{7a}$$

$$\partial_t V_n + c\partial_k I_n = 0, \quad \text{for TM modes.} \tag{7b}$$

The Laplace transform $\mathcal{L}$ of (6), assuming vanishing initial conditions, yields

$$\left(s^2 + \lambda_n^2 c^2 - c^2 \partial_k^2\right) \hat{f}_n = 0 \tag{8}$$

where $\hat{f}_n = \mathcal{L}(f_n)$, which can be factored as

$$(\beta - c\partial_k)(\beta + c\partial_k)\hat{f}_n = (\beta + c\partial_k)(\beta - c\partial_k)\hat{f}_n = 0 \tag{9}$$

where $\beta = (s^2 + \lambda_n^2 \, c^2)^{1/2}$.

Now, define

$$V_n^+ = \frac{V_n + \mathcal{Z}_n I_n}{2} \tag{10a}$$

$$V_n^- = \frac{V_n - \mathcal{Z}_n I_n}{2} \tag{10b}$$

where $\mathcal{Z}_n f$ is a (convolution) impedance operator, defined through its Laplace transform

$$\mathcal{L}\left(\mathcal{Z}_n f\right) = \begin{cases} \dfrac{s}{\beta}\hat{f}, & \text{for TE modes} \\ \dfrac{\beta}{s}\hat{f}, & \text{for TM modes.} \end{cases} \tag{11}$$

Operator $\mathcal{Z}_n$ corresponds, in the frequency domain, to the modal impedance normalized with respect to η [39, Sec. 3.3].

First, note that definition (10) entails a splitting

$$V_n = V_n^+ + V_n^- \tag{12}$$

of the modal voltages. We will show that $V_n^\pm$ individually satisfy the Klein–Gordon equation and thus correspond to valid solutions of the Maxwell equations in the waveguide.

For this, apply the Laplace transform to definitions (10), multiply both sides with $(\beta \pm c\partial_k)$, and use expression (11) and the Laplace transform of (7) to find that

$$(\beta \pm c\partial_k)\hat{V}_n^{\pm} = \frac{(\beta \pm c\partial_k)(\beta \mp c\partial_k)\hat{V}_n}{2\beta} = 0 \quad \text{for TE modes} \tag{13a}$$

$$(\beta \pm c\partial_k)\hat{V}_n^{\pm} = \frac{\pm(\beta + c\partial_k)(\beta - c\partial_k)\hat{I}_n}{2s} = 0 \quad \text{for TM modes} \tag{13b}$$

where the last equality in each case follows from factorization (9). Equation (13) shows that $V_n^{\pm}$ satisfy the Klein–Gordon equation. Crucially, as pointed out by Kristensson [38], this modal voltage splitting implies a division in parts of the field propagating in the positive (V_n^+) and negative (V_n^-) $\hat{\mathbf{k}}$ directions, respectively.

Similarly, we may split the modal currents into directional currents

$$I_n = I_n^+ + I_n^- \tag{14}$$

where

$$I_n^+ = \frac{I_n + \mathcal{Y}_n V_n}{2} \tag{15a}$$

$$I_n^- = \frac{I_n - \mathcal{Y}_n V_n}{2} \tag{15b}$$

in which $\mathcal{Y}_n$ is a convolution operator defined by its Laplace transform

$$\mathcal{L}(\mathcal{Y}_n f) = \begin{cases} \dfrac{\beta}{s}\hat{f}, & \text{for TE modes} \\ \dfrac{s}{\beta}\hat{f}, & \text{for TM modes} \end{cases} \tag{16}$$

which, in the frequency domain, corresponds to the modal admittance normalized by $1/\eta$. We remark the duality of the modal impedance (11) and admittance (16).

Time-domain expressions for these operators, assuming that they act on functions that vanish for $t \leq 0$, can be written as [23], [40], [41]

$$\mathcal{Z}_n^{\mathrm{TE}} f_n = \mathcal{Y}_n^{\mathrm{TM}} f_n = \mathcal{L}^{-1}\left[1 - (1 - \frac{s}{\beta})\right] * f_n = f_n - \lambda_n c J_1(\lambda_n c\cdot) * f_n \tag{17a}$$

$$\mathcal{Y}_n^{\mathrm{TE}} f_n = \mathcal{Z}_n^{\mathrm{TM}} f_n = \mathcal{L}^{-1}\left[1 - 1 + \frac{s}{\beta} + \frac{(\lambda c)^2}{s\beta}\right] * f_n = f_n - \lambda_n c J_1(\lambda_n c\cdot) * f_n + (\lambda_n c)^2 F * f_n \tag{17b}$$

where

$$F(t) = \int_0^t J_0(\lambda_n c\tau)d\tau \tag{18}$$

and where J_1 and J_0 are the first- and zeroth-order Bessel functions of the first kind, respectively.

In our computations, we set $V_n^+ = g$ as a boundary condition at the ports, where $g = 0$ at Port_2, and g at Port_1 is a signal with a spectral content covering the frequency interval of interest. In this way, the part of the fields propagating into the waveguide is prescribed, and the part that propagates out of the port, V_n^- and I_n^-, is left unaffected, creating matched port conditions.

The transmission and reflection properties of the device are in the optimization represented by portal quantities revealing the energy content of the modal waves, V_n^- and I_n^-, propagating out of the ports. By the orthogonality of the modal basis functions, and assuming that the fields vanish outside of the time interval $(0, T)$, the net energy flux through Port_i in direction $\hat{\mathbf{k}}$ can be written

$$W_i = \int_0^T \int_{\mathrm{S}} \hat{\mathbf{k}} \cdot (\mathbf{E} \times \mathbf{H}) d\mathrm{S} dt = \sum_{n=1}^{\infty} W_{i,n} \tag{19}$$

where

$$W_{i,n} = \int_0^T V_{i,n} I_{i,n} dt. \tag{20}$$

Note that W_i and $W_{i,n}$ are signed quantities, where the sign indicates the direction of the net energy flow with respect to $\hat{\mathbf{k}}$.

Substituting the splittings (12) and (14) into expression (20), we find that the net energy flux of mode n satisfies

$$W_{i,n} = W_{i,n}^+ + W_{i,n}^- + W_{i,n}^{\mathrm{s}} \tag{21}$$

where

$$W_{i,n}^+ = \int_0^T V_{i,n}^+ I_{i,n}^+ dt \tag{22a}$$

$$W_{i,n}^- = \int_0^T V_{i,n}^- I_{i,n}^- dt \tag{22b}$$

$$W_{i,n}^{\mathrm{s}} = \int_0^T V_{i,n}^+ I_{i,n}^- dt + \int_0^T V_{i,n}^- I_{i,n}^+ dt. \tag{22c}$$

Expression (21) decomposes the energy at Port_i into the sum of the imposed energy $W_{i,n}^+$, the outgoing energy $W_{i,n}^-$, and the mixed energy $W_{i,n}^{\mathrm{s}}$. The outgoing energy $W_{i,n}^-$ will be utilized in the optimization to maximize transmission and minimize reflection.

Remark 1: The mixed energy $W_{i,n}^{\mathrm{s}}$ term is due to the dispersive nature of hollow waveguides, and its presence is a consequence of the fact that the modal impedance $\mathcal{Z}_n$ is a convolution operator. Note that the mixed energy vanishes when either $V_{i,n}^+$ and $I_{i,n}^+$ or $V_{i,n}^-$ and $I_{i,n}^-$ vanish. Moreover, for nondispersive transmission lines supporting TEM waves, and in the case of single-frequency time-harmonic waves, the impedance operator $\mathcal{Z}_n$ reduces to multiplication with a real or complex number. In that case, there is no mixed energy term. Thus, although the modal voltage and current can be split into waves propagating in the positive and negative directions, according to (12) and (14), the energy flux does not split in exactly the same way. Nevertheless, numerical evidence indicates that the mixed energy term tends to be orders of magnitude smaller than the other terms. In the current setup, the mixed energy term is about 0.5 % of the imposed signal in the worst case. Therefore, we will ignore this term in the optimization problem formulation, as indicated in the following.

B. Problem Formulation

For the setup shown in Fig. 1, as discussed earlier, we impose boundary conditions on V_n^+ at both ports. We prescribe a vanishing V_n^+ at Port_2 and a nonzero signal g with a given frequency content at Port_1. The frequency content of g is such that only the first mode (TE_{10}) propagates both in the SIW and the RWG. However, higher modes can be expected to be generated by the transition region, leaking into the waveguides, which is why we consider the first three modes in the boundary conditions in order to absorb any residual evanescent waves at the ports. Thus, the imposed boundary conditions mean that both ports experience matched conditions.

In the transition section, we expect ohmic losses

$$W_{\text{loss}} = W^{\Omega} + W^{\text{c}} + W^{\text{d}} \tag{23}$$

where W^{Ω} is the loss in the copper sheets to be designed, W^{c} is the loss in the waveguide conductive walls, and W^{d} is the dielectric substrates' loss. The energy losses in $\mathbf{\Omega}$ can be computed by

$$W^{\Omega} = \int_{\Omega}\int_{0}^{T} \sigma \mathbf{E}^2 \; dt d\Omega. \tag{24}$$

We assume that the fields, and thereby the energy inside the domain, vanish outside the time interval $(0, T)$. Energy conservation then yields to balance law

$$W_{1,1} = W_{\text{loss}} + |W_{2,1}| \tag{25}$$

that is, the net energy flux into Port_1 either ends up as losses or flows out through Port_2. (The absolute value is inserted to make all terms nonnegative.) Inserting the energy split (21) into energy balance (25), we find

$$\begin{aligned} W_{1,1}^{+} &= \left|W_{1,1}^{-} + W_{1,1}^{s}\right| + W_{\text{loss}} + \left|W_{2,1}^{-}\right| \\ &\approx \left|W_{1,1}^{-}\right| + W_{\text{loss}} + \left|W_{2,1}^{-}\right| \end{aligned} \tag{26}$$

using that $W_{2,1}^{+} = W_{2,1}^{\text{s}} = 0$ and ignoring the mixed energy term in (26).

A natural and simple statement of the optimization problem is to fix the incoming signal, and thus the imposed energy $W_{1,1}^{+}$ at Port_1, and to seek a spatial distribution of the copper in $\mathbf{\Omega}$ to maximize the transmission term $|W_{2,1}^{-}|$ at Port_2. From energy balance (26) it then follows, since the left side is constant, that maximization of the transmission automatically leads to a minimization of the two other terms: the reflected energy at Port_1 and the losses.

Another possibility is instead to minimize the reflected energy $|W_{1,1}^{-}|$ at Port_1. Energy balance (26) implies that the sum of the transmission term $|W_{2,1}^{-}|$ and the loss term W_{loss} will then be maximized. Taken by itself, this approach seems not as favorable as the previous one due to the implicit maximization of losses. However, in previous work concerning antenna optimization [42], we noticed that the combination of maximizing the transmission energy and minimizing the reflected energy resulted in optimized designs with a more even performance over the frequency band of interest compared to when only the transmission energy was maximized, that is, the final designs typically possess a performance that compromises between a high transmission and a low reflection over the entire band of interest, which is typically required for many systems operating over wide frequency bands.

However, when using the same concept in this article, we experienced in-band resonance issues in many of the optimized designs [34]. One explanation for these resonance issues is that due to the high permittivity and the complex structures created in the transition, cavity regions of the transition will be subject to higher order modes. If this region includes a structure that resonates at a certain frequency, the energy carried by this frequency will be trapped in the structure, but the portal quantities only may not be able to easily detect such internal resonances. However, for a lossy structure, the ohmic losses in the structure would likely increase at the resonance frequency. As will be described in detail next, during the optimization process, the design evolves through a sequence of lossy structures. Thus, adding the minimization of the ohmic losses W^{Ω} to the optimization problem formulation increases the sensitivity to resonances in the transition and makes the optimized designs less prone to resonances. This issue is illustrated through numerical experiments in Appendix A. Therefore, we formulate the optimization problem as

$$\begin{aligned} &\min_{\boldsymbol{\sigma}\in\mathcal{U}} \; \log\left(\frac{W_{1,1}^{-} W^{\Omega}}{|W_{2,1}^{-}|}\right) \\ &\text{s. t. the governing equations,} \\ &\qquad \text{imposed energy flux } W_{1,1}^{+} \end{aligned} \tag{27}$$

where $\mathcal{U}$ is the admissible set of conductivities, described in detail in the discrete case next.

C. Numerical Treatment

We numerically solve the governing equations (1) by the FDTD method [43] using our custom software. The analysis domain is discretized by a uniform cubical grid with a spatial cell size Δ and a time step Δt. The modal voltages V_n and currents I_n are computed at the waveguide ports based on discrete versions of integrals (5) and the FDTD discretization of $\mathbf{E}$ and $\mathbf{H}$, respectively. More precisely, the discretization of the modal voltages and currents uses the staggered grids in space and time that are employed by the Yee scheme. Moreover, the traveling waves defined in expressions (10) and (15) are approximated at Port_i and time step m by

$$V_{i,n}^{\pm m}(k_i) = \frac{V_{i,n}^{m}(k_i) \pm \mathcal{Z}_{i,n} I_{i,n}^{\left(m-\frac{\Delta t}{2}\right)}\left(k_i + \frac{\Delta}{2}\right)}{2} \tag{28a}$$

$$I_{i,n}^{\pm m}\left(k_i + \frac{\Delta}{2}\right) = \frac{I_{i,n}^{\left(m-\frac{\Delta t}{2}\right)}\left(k_i + \frac{\Delta}{2}\right) \pm \mathcal{Y}_{i,n} V_{i,n}^{m}(k_i)}{2}. \tag{28b}$$

Similarly, energy terms (22b) and (24) are discretized to compute the terms of the objective function.

At Port_1, $V_{1,1}^{+m}$ is set to a truncated, time-sampled sinc signal, covering the frequency band of interest, and, at Port_2, $V_{2,1}^{+m}$ is set to vanish. The admittance and impedance operators are discretized in a straightforward way consistent with the discrete modal voltages and currents. The discretized unknown conductivities are vectors $\boldsymbol{\sigma}$ of the conductivities σ_i at each Yee edge in $\mathbf{\Omega}$.

D. Density-Based Topology Optimization

To solve the discrete version of problem (27), we use a density-based topology optimization (DBTO) approach [28], [29]. In DBTO, the design domain Ω is divided into small elements. A vector $\mathbf{p}$ of binary design variables p_i marks, for each element, presence, $p_i = 1$, or absence, $p_i = 0$, of the material, here copper. This type of geometry description leads to a large-scale, nonlinear integer optimization problems. To avoid solving such computationally intractable problems, the DBTO approach is to relax the integer constraint and allow the design variables to vary continuously between 0 and 1. This relaxation of the design variables enables the use of gradient-based optimization methods to efficiently solve topology optimization problems where the design vector $\mathbf{p}$ may hold thousands, millions, or even billions of entries [27], [44]. Although the design variables are allowed to vary continuously during the optimization process, a penalty approach is used so that the final design vector approximately holds the binary values in order to obtain a manufacturable design. To map between the density variable p_i and the physical conductivity, we use the mapping

$$\sigma_i = 10^{8p_i-3} \quad \text{(S/m)} \tag{29}$$

where the coefficients 8 and 3 are chosen based on numerical investigations. The mapping (29) interpolates exponentially between a good conductor ($\sigma_{\max} = 10^5$ S/m) and a good dielectric ($\sigma_{\min} = 10^{-3}$ S/m).

One issue with the relaxation of the design variables is that intermediate values (that is, values of p_i between 0 and 1) impose ohmic losses in the design domain. As noted in Section III-B, when maximizing the transmitted energy, the loss term is automatically minimized, which makes the current optimization problem self-penalizing toward the lossless case (that is, toward $p_i = 1$ or $p_i = 0$). (In other applications, an explicit penalty procedure has to be used in order to promote final binary values of the design.) The self-penalization is useful at the end of the optimization procedure, but if not modified, it tends to aggressively terminate the optimization quickly, resulting in designs with poor performances [45]. To mitigate the self-penalization, a blurring filter can be imposed on the design variables [34], where each element value is replaced by a weighted average of the neighboring elements' values, that is, we replace $\mathbf{p}$ in (29) by

$$\tilde{\mathbf{p}} = \mathbf{F}\mathbf{p} \tag{30}$$

where matrix $\mathbf{F}$ determines the action of a blurring filter on the design variables $\mathbf{p}$. To obtain a lossless final design, the blurring of the design variables is removed through a continuation approach over the filter radius. More precisely, we use a sequence of decreasing filter radii, $R_1 > R_2 > \cdots > R_N$. At subproblem i, we use a filter matrix $\mathbf{F}^{(i)}$ corresponding to the filter radius R_i. (We remark that, here, we select R_N sufficiently small so that $\mathbf{F}^{(N)} = \mathbf{I}$.) For each experiment, the initial design is specified in Section IV. As initial guess for subproblem $i+1$, where $i \geq 1$, we adjust $\mathbf{p}$ to obtain the same physical design as the optimized physical design from subproblem i, that is, $\tilde{\mathbf{p}}_{\text{init}}^{(i+1)} = \tilde{\mathbf{p}}_{\text{opt}}^{(i)}$.

The topology optimization problem after discretization is

$$\begin{aligned} \min_{\boldsymbol{p}} \quad & \log\left(\frac{\tilde{W}_{1,1}^{-}\tilde{W}^{\Omega}}{|\tilde{W}_{2,1}^{-}|}\right) \\ \text{s. t. the governing equations,} & \\ \text{the imposed energy } & \tilde{W}_{1,1}^{+} \end{aligned} \tag{31}$$

where the tilde symbol indicates the numerical approximation of the corresponding terms. To solve optimization problem (31), we employ the GCMMA algorithm [46]. The GCMMA is a gradient-based optimization method suitable to solve large-scale optimization problems.

One approach to compute the gradient vector is to use finite differences. For large-scale problems, however, this approach is computationally inefficient. An alternative is to use the adjoint-field methods, which typically allow the computation of the gradient vector by one additional simulation per observation [47].

We use the adjoint-field method to compute the gradient of the objective function. The objective function comprises three terms that are observed at different locations in space. This makes it possible to rely on the linearity of Maxwell's equations and solve only one adjoint system with three excitations. More precisely, the outgoing signal of (10b) at Port_1 and Port_2 together with the electric field in the design domain is recorded, reversed in time, and used to feed the adjoint system [48]. The gradient of $W_{i,n}$ can be computed by using

$$\frac{\partial W_{i,n}}{\partial \sigma_e} = -\Delta^3 \sum_{m=1}^{N} E_e^{N-m} \frac{E_e^{*m-\frac{1}{2}} + E_e^{*m+\frac{1}{2}}}{2} \Delta t \tag{32}$$

where e is the index for an arbitrary Yee edge inside the design domain, N is the number of time steps in the simulation, E_e is the discrete electric field obtained by the FDTD solution to (1), and E_e^* is a discrete adjoint electric field obtained by solving the adjoint system. Compared to (32), the gradient expression of W^{Ω} includes one additional term that can be explicitly computed (see Appendix B). Thus, for any number of design variables, the computation of the objective function gradient requires only two FDTD simulations. The flowchart in Fig. 3 summarizes the optimization algorithm.

IV. Numerical Results

We design a transition between a WR42 waveguide with a cross section 10.668 mm × 4.318 mm and an SIW with $w_s = 5.5$ mm, $q = 0.6$ mm, and $d = 0.4$ mm, as shown in Fig. 1. The three-layer substrate comprises two Rogers RO4350B substrates (cores) and one FR4-substrate (prepreg). The cores have the height $h_c = 0.254$ mm, dielectric constant $\varepsilon_c = 3.66$, and loss tangent $\tan\delta = 0.0037$ at 10 GHz. The prepreg has $h_p = 0.48$ mm, $\varepsilon_p = 4.2$, and $\tan\delta = 0.015$ at 10 GHz. The estimated thicknesses of the copper sheets are 18 and 35 μm for the inner and outer sheets, respectively. At Port_2, we terminate the SIW by using a smooth sidewall of length $l_p = 2q$, as shown in Fig. 1(a), where the dielectric substrate is assumed loss-free. For the WR42 and the SIW, the dominant TE_{10} mode propagates between the first and second cutoff frequencies, which are 14.05 and 28.10 GHz

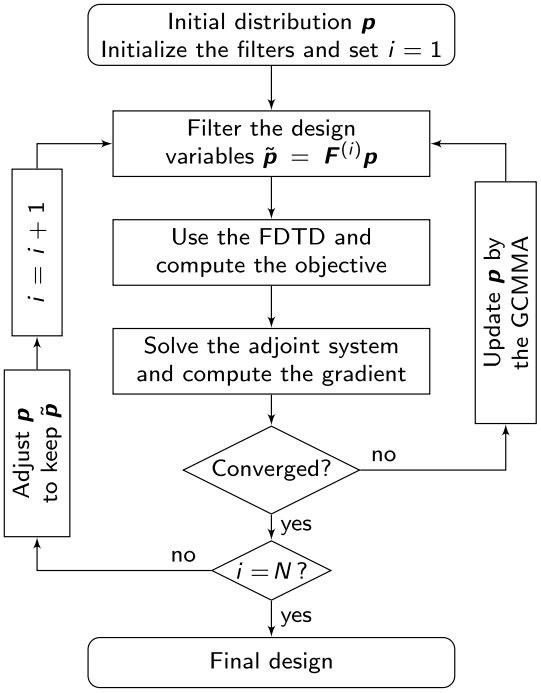

Fig. 3. Flowchart of the optimization algorithm.

Fig. 4. Initial design variables and its corresponding filtered designs over the three-layer design domain, arranged from bottom to top.

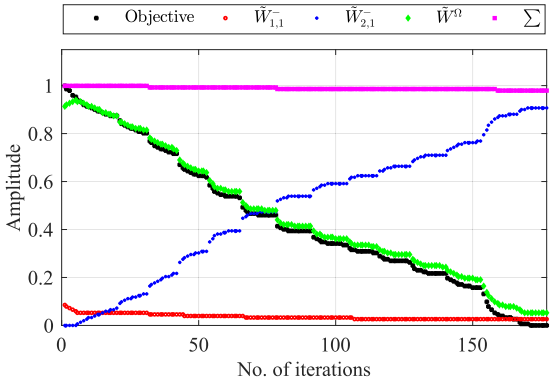

Fig. 5. Development of the objective function, the three terms comprising the objective function, and their sum versus the number of iterations.

for the WR42 and estimated to be 15.09 and 30.18 GHz for the SIW [49], respectively. The frequency band of interest is 18–28 GHz.

In the FDTD simulations, we use $\Delta = 0.0508$ mm and Δt equals 0.85 of the Courant limit. As an excitation signal, we use a sinc signal truncated after seven sidelobes to modulate a 23-GHz carrier and cover the frequency band of interest. The computational domain is terminated by a uniaxial PML in the y and positive z directions. The FDTD code is implemented to run on graphics processing units (GPUs), and the computations are carried out on nodes equipped with NVidia V100 GPUs and 64 GB of memory. For the chosen discretization, the number of design variables is 105 960, which corresponds to the interior Yee edges in the design domain Ω. The simulation time of one FDTD simulation is approximately 3 min. To compute the objective function gradient, we store the electric field in the design domain at each time step both for the original and the adjoint-field problems. For the chosen discretization, this field storage requires at most 52 GB of memory.

Typically, in topology optimization problems, a uniform initial distribution of the design variables is used. However, the current problem setup entails the nonuniform sensitivities of the objective function to the design variables. More precisely, the SIW is connected along the sidewall of the RWG. This setup makes the objective function severely sensitive to design variables near the interface between the transition and the SIW compared with design variables at other regions in the design domain. Starting with a uniform distribution in this case, the design algorithm removes any material at the interface between the SIW and the transition region and converges to local optima with poor performance. This may be explained as follows. At the beginning of the optimization, the transmission term $|\tilde{W}^{-}_{2,1}|$ is very small. Based on the logarithmic function in (31), the contribution of $|\tilde{W}^{-}_{2,1}|$ to the objective function gradient is inversely proportional to its amplitude. Therefore, the transmission term $|\tilde{W}^{-}_{2,1}|$ is prioritized at the beginning of the optimization. One way to maximize $|\tilde{W}^{-}_{2,1}|$ is to remove lossy material from the path of the signal between Port_1 and Port_2. In other words, the algorithm quickly drives toward a lossless design close to this interface, which increases the likelihood of becoming trapped in a poor local optimum. Therefore, to help the design algorithm in avoiding such poor local optimum, we chose to start the optimization with the initial design and its corresponding filtered designs shown in Fig. 4. By this choice, the initial design contains regions with good conductor (black color), good dielectric (white color), and intermediate material (gray color). Note the choice of a good conductor of the bottom layer that connects to the SIW at the left side.

Fig. 5 shows the progress of the objective function and its components versus the number of iterations. The objective function is monotonically decreasing. There are some jumps between the consecutive subproblems where the number of filter cascades is decreased. As can be noted from the objective function curve, there are 14 subproblems, and the algorithm converged after 177 iterations. The GCMMA used a total of 398 solutions of Maxwell's equations to evaluate the objective function and the required gradient information during the optimization process, that is, on average, the GCMMA used 2.25 calls to the Maxwell solver per iteration. Energy balance (26) shows that the sum of the loss term plus the reflected and transmitted energy term should be constant, up to the minor approximation of ignoring the mixed energy term. Fig. 5 reveals that the evolution of the sum Σ of the absolute

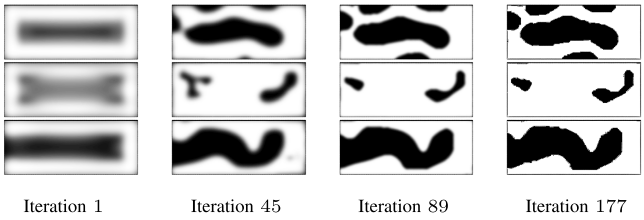

Fig. 6. Filtered (physical) designs at iterations 1, 45, 89, and 177.

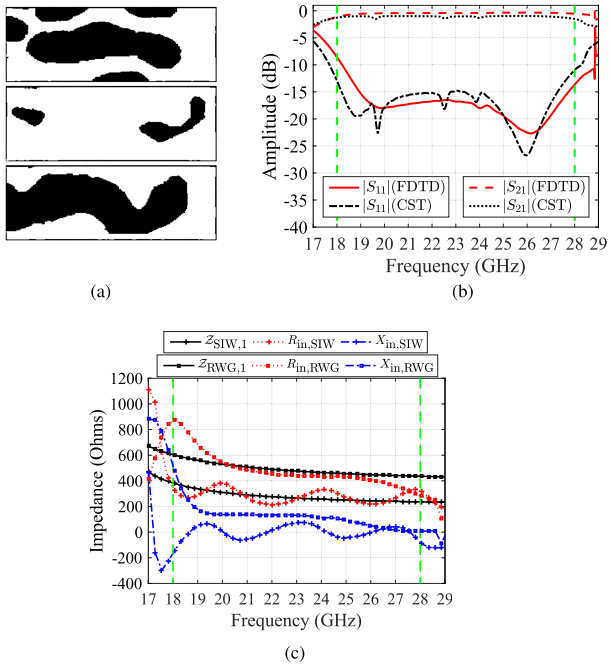

Fig. 7. Transition I. (a) Final optimized design. (b) Scattering parameters of the design compute by using the FDTD method and compared with the CST package. (c) Input impedance of the transition seen from the SIW side and from the RWG side compute by using the FDTD method, regarding the first propagating mode. The modal impedances inside the SIW and the RWG are given as references. The vertical dashed lines mark the frequency band of interest 18–28 GHz.

values of the objective function components stays essentially constant. The slight decrease during the iterations, less than 2%, is likely due to the increase in dielectric/metallic losses $W^{\mathrm{c}}+W^{\mathrm{d}}$ in the SIW as the amplitude of the waves transmitted through the device increases.

Fig. 6 shows the filtered designs at selected iterations, depicting the evolution of the layout of the three layers. Note the large areas of gray at the early stage of optimization, that the amount of grayness successively decreases, and that finally small details and crisp boundaries between a good conductor (black) and good dielectric (white) appear.

Fig. 7(a) shows the final optimized copper distribution over the three layers. We denote this design as Transition I. Fig. 7(b) shows the computed scattering parameters of the final design. The computed scattering parameters are cross-verified by the commercial CST Microwave Studio package. The optimized transition has a reflection coefficient $|S_{11}|$ below -10 dB over the entire frequency band of interest and -15 dB over 90% of the frequency band of interest. Moreover, the computed transmission coefficient $|S_{21}|$ is above -1 dB over the entire

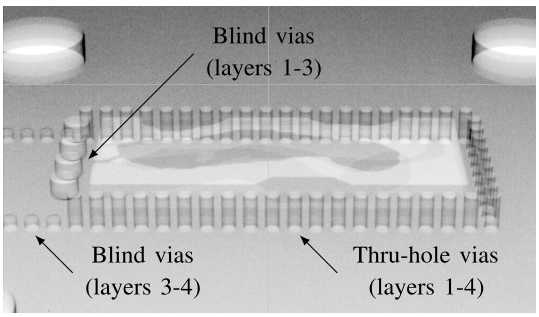

Fig. 8. X-ray image (side view) of a manufactured transition showing the different types of vias.

frequency band of interest. The slight differences between the computed results by our FDTD method and by the CST package could be ascribed to differences in geometry description of the two methods. We remark that the insertion loss includes the losses of a 10-mm RWG and a 9.0-mm SIW that are used as waveguide ports. Fig. 7(c) shows the computed input impedance of the transition seen from the SIW side and from the RWG side, regarding the first propagating mode. The modal impedances of the SIW and the RWG versus frequency are given as references in Fig. 7. Note that these impedances are not normalized with respect to η, in contrast to the discussion in Section III-A.

V. Stack-Up and Manufacturing Process

The optimized transitions were fabricated in a back-to-back configuration by Rohde & Schwarz, Teissnach, Germany. Therefore, two Rogers RO4350B cores with a thickness of 254 μm each were stacked on top of each other with three prepreg layers (490 μm in sum) in between. The expected fabrication tolerance in shaping the boundaries of the optimized copper sheets is ± 10 μm, which is much smaller than the spatial discretization step used in this article ($\Delta = 50.8$ μm). The blind vias limiting the SIW were drilled into the bottom Rogers core before the lamination process. Afterward, thru-hole vias limiting the cavity below the RWG were drilled. The special blind vias connecting copper layers 1–3, and hence limiting the cavity in the top core and the prepreg material, were carefully drilled such that the bottom core remains unaffected. Due to constraints of the fabrication process, we use blind vias with a diameter $d = 0.8$ mm and a center-to-center separation $q = 1.2$ mm. A manufacturing tolerance in drilling the blind vias height is expected, which is further investigated in Section VI. In the last step, a silver coating was added by chemical deposition. The manufacturing process was validated by the X-ray image shown in Fig. 8.

VI. Measurement Results

The measurements of the back-to-back transitions were performed with an Agilent PNA-X N5244A vector network analyzer (VNA) and used the setup shown in Fig. 9. Before the actual measurement, the VNA was calibrated in the frequency range of interest with the short, line, and through method at the end of the waveguides. Fig. 10(a) shows a photograph

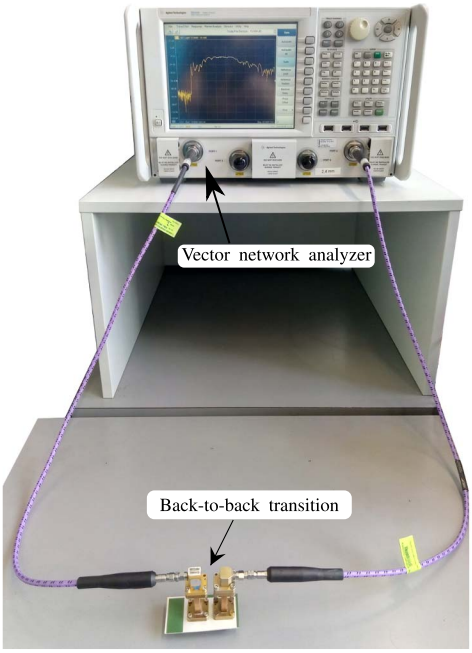

Fig. 9. Measurement setup for determining the S-parameters of the back-to-back transitions.

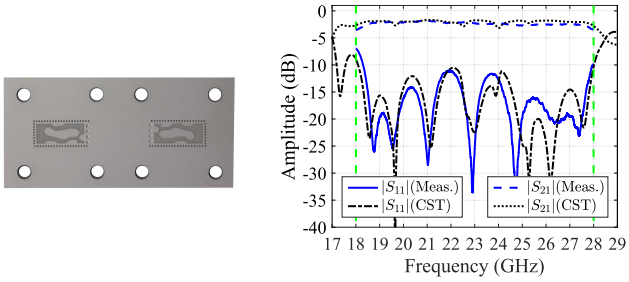

Fig. 10. (a) Photograph of the manufactured back-to-back prototype of Transition I. (b) Measured and simulated scattering parameters of the back-to-back prototype. The vertical dashed lines mark the frequency band of interest 18–28 GHz.

of the manufactured back-to-back prototype. Fig. 10(b) shows the measured scattering parameters of the manufactured back-to-back prototype together with the CST simulated results. There is a good match between the measurements and the simulated results. The measured $|S_{11}|$ is essentially below -10 dB and the $|S_{21}|$ curve is above -2.5 dB over the entire band of interest 18–28 GHz. We remark that these scattering parameters correspond to the two transitions and a 16-mm SIW section in between.

As a second numerical experiment, we solve the optimization problem (31) with the RWG rotated 90° around its axis, that is, the center of the SIW is aligned to the center of the broad sidewall of the RWG (see Fig. 1). We solve the optimization problem with the same settings as in the previous case. Fig. 11(a) and (b) shows the initial and final designs, respectively. We denote this design as Transition II. The computed scattering parameters of the final design are shown in Fig. 11(c). Fig. 11(d) shows a photograph of the back-to-back prototype. The measured back-to-backscattering parameters, cross-verified with the CST simulations,

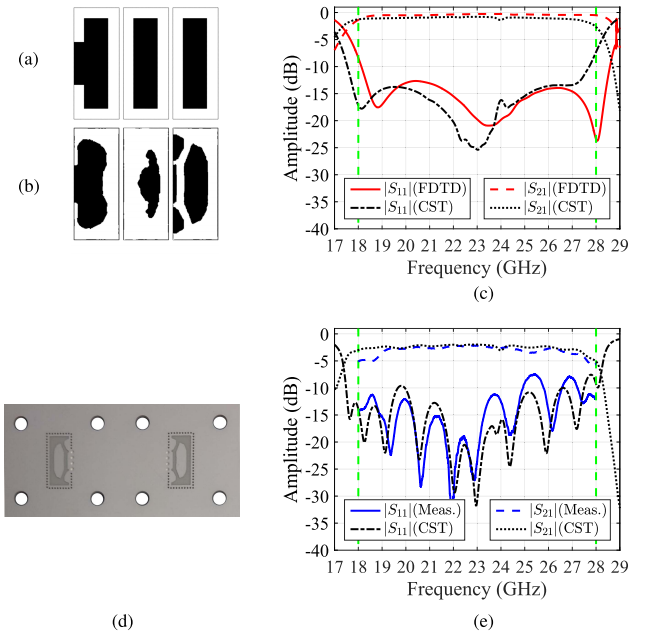

Fig. 11. Transition II. (a) and (b) Initial and final optimized design, respectively, when the RWG is rotated by 90° around its axis. (c) Simulated scattering parameters of the transition compute by using the FDTD method and compared with the CST package. (d) Photograph of the manufactured back-to-back prototype. (e) Measured scattering parameters of the back-to-back prototype.

are plotted in Fig. 11(e). The design is essentially symmetric around the SIW axis. We note a decrease in the measured $|S_{21}|$ at the lower side of the frequency band, which will be discussed further in the following.

As a final experiment, we solve the previous problem when the SIW–RWG interface is moved to the edge of the RWG broad sidewall. In this case, the RWG is rotated 90° around its axis, and the sidewall of the cavity region and the sidewall of the SIW are aligned. Fig. 12(a) and (b) shows the initial design and final optimized design for the new configuration. We denote this design as Transition III. The computed scattering parameters of this configuration are shown in Fig. 12(c). The transition has a computed $|S_{11}|$ below -15 dB and $|S_{21}|$ above -1 dB over the entire frequency band of interest. Fig. 12(d) shows a photograph of the manufactured back-to-back transition, and the measured scattering parameters are shown in Fig. 12(e). The manufactured back-to-back prototype shows $|S_{11}|$ below -10 dB and a corresponding $|S_{21}|$ above -2.5 dB over the entire frequency band of interest.

We assess the impact of the manufacturing tolerance of the blind vias on the performance of the three presented configurations. We define a parameter h_t that varies between zero and h_p; $h_t = 0$ indicates a direct contact between the blind vias and the second copper foil, and $h_t = h_p$ indicates an open wall between the transition cavity and the prepreg layer [see Fig. 1(b)]. Fig. 13(a)–(c) shows the change in the scattering parameters of the three configurations when the parameter h_t varies from 0 mm to 0.411 mm with a step of 0.067 mm. The results of the first configuration (Transition I) presented in Fig. 13(a) show the smallest changes in the scattering parameters as the connection of the blind vias and the ground plane is perturbed. Fig. 13(b) shows that the second

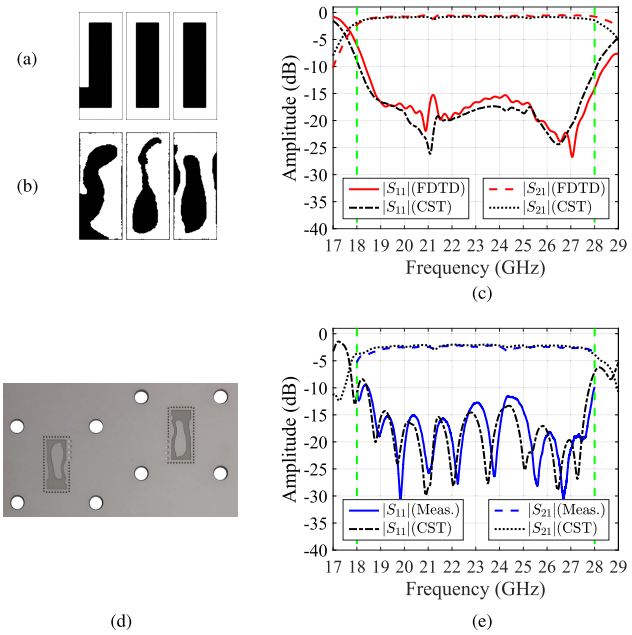

Fig. 12. Transition III. (a) and (b) Initial and final optimized design, respectively, when the SIW–RWG interface is moved to the lower side. (c) Simulated scattering parameters of the transition compute by using FDTD and compared with the CST package. (d) Photograph of the manufactured back-to-back prototype. (e) Measured scattering parameters of the back-to-back prototype.

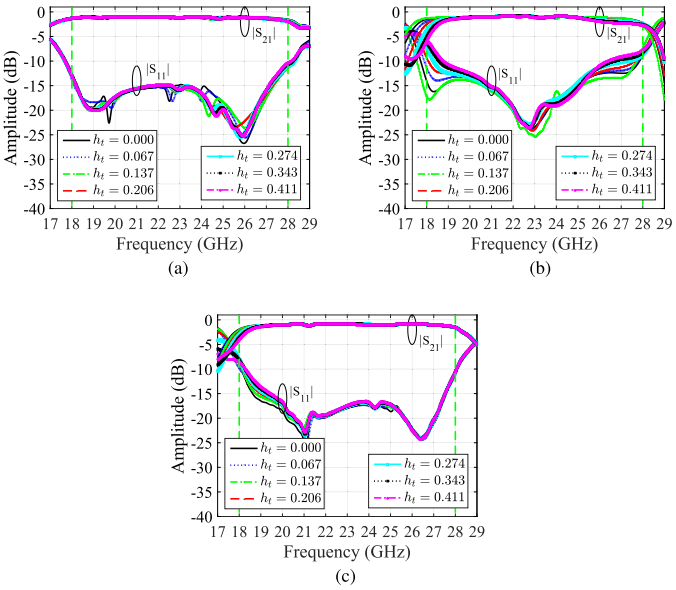

Fig. 13. Sensitivity of the scattering parameters to connection tolerance of the blind vias of (a) Transition I (see Fig. 7), (b) Transition II (see Fig. 11), and (c) Transition III (see Fig. 12).

configuration (Transition II) is sensitive to tolerances in the blind vias both at the lower and upper frequencies inside the frequency band of interest. Fig. 13(c) shows that the third configuration (Transition III) exhibits small changes in its scattering parameter only close to the lower frequencies. Based on this assessment, we anticipate that the discrepancies between the simulations and the measurements in Fig. 11(e), at the lower frequencies, can be attributed to the manufacturing tolerance of the blind vias.

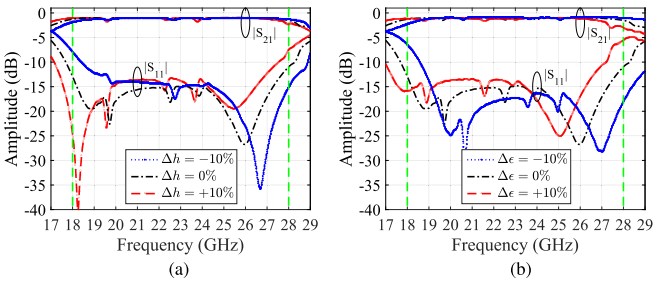

Fig. 14. Sensitivity of the scattering parameters of Transition I (see Fig. 7) under $\pm 10\%$ perturbations in (a) heights and (b) complex permittivities of the cores and the prepreg substrates.

The performance of planar devices is sensitive to the parameters of the hosting substrates. Here, we demonstrate the impact of the substrates parameters on the scattering parameters of the optimized transitions. We perturb the thickness and the complex permittivity of the employed substrates by $\pm 10\%$ of their design values. For brevity, we demonstrate this study on Transition I. Fig. 14(a) shows the change in the scattering parameters of Transition I under $\Delta h = \pm 10\%$ perturbations in the thicknesses of the cores and the prepreg substrates. Compared to the reference design ($\Delta h = 0$), the 10% increase (decrease) in the thicknesses of the substrates improves the transition performance at the lower (higher) band edge, while the performance slightly deteriorates at the higher (lower) band edge. On the other hand, the increase (decrease) in the value of the substrates' permittivities only shifts the transition performance toward lower (higher) frequencies, as shown in Fig. 14(b). At the center of the frequency band of interest, the performance of the transition is less sensitive to perturbations in the parameters of the substrate. Overall, the differences between the curves for the different perturbations in Fig. 14 are significantly larger than the difference between the two curves for the simulated and measured scattering parameters in Fig. 10.

VII. Discussion

Table I summarizes and compares our results with other state-of-the-art approaches. It can be seen that many published devices show low insertion and return loss but are either difficult to align or very costly even for a high-volume market. In some of the use cases, they may still be feasible, due to their low losses; however, high effort and cost is a knockout criterion for low-cost applications, such as industrial radar systems. Furthermore, the transitions proposed here are comparably insusceptible to alignment tolerances. With the measurement results of two transitions with different SIW lengths, the insertion loss of a single transition was determined to be less than 1 dB in the given frequency range.

For the optimization of the three configurations presented earlier, each layer starts with one block of material. Then, the algorithm is able to modify the boundaries of the initial design, create new blocks of material, or split the existing ones. (That is, the final topology—how parts are connected—can drastically be changed compared to the initial design.) Changes of such design features can be difficult to achieve

TABLE I
COMPARISON OF DIFFERENT SIW-TO-RWG TRANSITIONS

Reference	Bandwidth	Center frequency	RL (dB)	IL (dB)	Transition type	Substrate height (guided wavelength)
[11]	$> 37\%$	22 GHz	> 11.9 dB	0.22 dB	3D-stepped transformer	0.055
[51]	$< 44\%$	90 GHz	> 10 dB	0.9 dB	Fin-line tapered transition	0.080
[52]	38%	61.8 GHz	> 15.6 dB	1.64 dB	Fin-line transition	0.077
[53]	17.5%	35.4 GHz	> 15 dB	0.6 dB	Planar structure+transformer	0.089
[54]	41%	33 GHz	> 15 dB	1.1 dB	Planar structure+transformer	0.129
[55]	38.8%	33.5 GHz	> 15 dB	0.51 dB	Planar structure+vias	0.248
[56]	48.5%	62.35 GHz	> 12 dB	0.5 dB	Planar structure+vias	0.181
This work	$> 43\%$	23 GHz	> 10 dB	< 1.0 dB	Optimized multi-layer planar structure	0.150

by the so-called shape optimization methods, where only the boundaries of a given shape are allowed to be modified. However, pixelating the design domain into a checkerboard of binary design variables and employing stochastic optimization methods such as genetic algorithms, it would be possible, in principle, to carry out a similar task as here. Unfortunately, stochastic optimization methods are computationally prohibitive to use for a large number of design variables; for such methods, the number of calls to the Maxwell solver is around two-to-three orders of magnitude higher than the number of design variables [45], [50]. Note that the current design problems involve 105 960 design variables, and they are solved using less than 400 calls to the Maxwell solver with our gradient-based approach. We remark that the current problem setup and its solution by the topology optimization approach could be extended with little effort to cover other frequency ranges.

VIII. CONCLUSION

This article presents a multilayer topology optimization approach to design planar transitions between an SIW and an RWG. Time-domain solutions of Maxwell's equations combined with boundary conditions based on the modal field analysis make it possible to efficiently simulate for wideband properties. The high dielectric constant and the complexity of the structure at the transition region make the device subject to develop in-band resonances during the optimization. Adding the minimization of the ohmic losses in the structure to the formulation of the objective function makes the final design less prone to the resonance issue. The algorithm optimizes the portal and in-domain quantities and reveals nonintuitive topologies. The effectiveness of the optimization algorithm is demonstrated through the optimization of the transition for different configurations with excellent results for each case.

APPENDIX

A. In-Band Resonance

This section presents two examples that illustrate the in-band resonance issue that typically appears if the ohmic losses' term is not included in the optimization problem formulation. Fig. 15 shows the final design and the scattering parameters when the same problems as presented in Fig. 7(a) and (b) are solved by the optimization algorithm without including the term $\tilde{W}^{\Omega}$. We note the presence of two

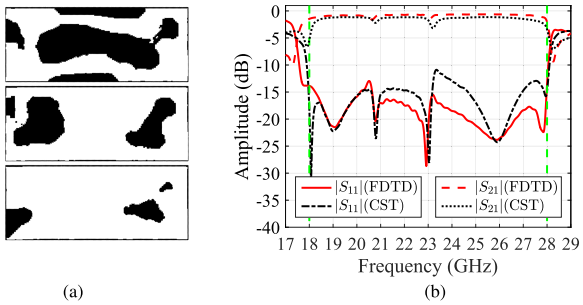

Fig. 15. (a) Final optimized design when the loss term $\tilde{W}^{\Omega}$ is not included in the optimization problem of the configuration presented in Fig. 7(a) and (b). (b) Scattering parameters of the optimized structure.

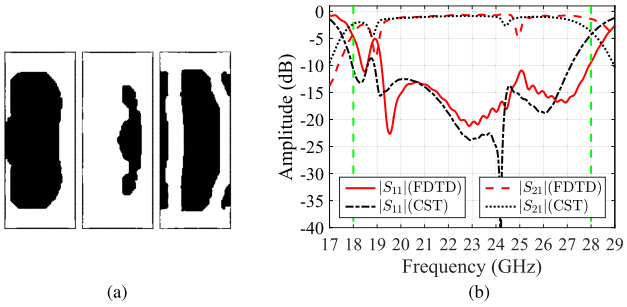

Fig. 16. (a) Final optimized design when the RWG is rotated by 90° around its axis and $\tilde{W}^{\Omega}$ is not included in the optimization. (b) Scattering parameters of the optimized structure.

in-band resonance close to the frequencies 21 and 23 GHz. Similarly, Fig. 16 shows the results of solving the same problem as shown in Fig. 11, but without including $\tilde{W}^{\Omega}$ in the optimization. Here, we observe two prominent resonances close to the frequencies 19 and 25 GHz. These results suggest that adding the minimization of $\tilde{W}^{\Omega}$ to the optimization problem formulation makes the final design less prone to in-band resonances.

B. Derivatives of Ohmic Losses

In this section, we present an adjoint system that allows the computation of the derivatives of the ohmic losses with respect to the conductivities. Let $\delta\sigma$ be a perturbation of the conductivity σ. By differentiating the objective function (24) with respect to the conductivity, we obtain

$$\delta W^{\Omega} = \int_{\Omega}\int_{0}^{T} \mathbf{E}^2\, \delta\sigma\, dt\, d\Omega + \int_{\Omega}\int_{0}^{T} 2\sigma\, \mathbf{E}\, \delta\mathbf{E}\, dt\, d\Omega \quad (33)$$

where δW^{Ω} and $\delta \mathbf{E}$ are the first variations of W^{Ω} and $\mathbf{E}$, respectively. The evaluation of the first term on the right-hand side of (33) is straightforward when the electric field at the domain $\mathbf{\Omega}$ is available from the original system (1). The second term can be evaluated by solving

$$\partial_t \varepsilon \mathbf{E}^* + \sigma \mathbf{E}^* - \nabla \times \mathbf{H}^* = 2\sigma \overleftarrow{\mathbf{E}} \tag{34a}$$

$$\partial_t \mu \mathbf{H}^* + \nabla \times \mathbf{E}^* = \mathbf{0} \tag{34b}$$

over the analysis domain and the time interval $(0, T)$, where $\overleftarrow{\mathbf{E}}$ is the electric field of the original system reversed in time, that is, $\overleftarrow{\mathbf{E}}(t) = \mathbf{E}(T - t)$. The adjoint system (34) allows replacing the second term on the right-hand side of (33) by

$$\int_{\Omega}\int_{0}^{T} 2\sigma \mathbf{E}\, \delta\mathbf{E}\; dt\, d\Omega = -\int_{\Omega}\int_{0}^{T} \overleftarrow{\mathbf{E}}\; \mathbf{E}^*\, \delta\sigma\; dt\;\; d\Omega. \tag{35}$$

The electric $\mathbf{E}^*$ and magnetic $\mathbf{H}^*$ fields of the adjoint system have zero initial values, and the adjoint system is complemented by the same boundary conditions as the original system (1). The right-hand side of (34a) represents an excitation to the adjoint system. We remark that this excitation has a nonzero value only at the design domain $\mathbf{\Omega}$. The detailed derivation of the adjoint system is similar to the one by Hassan *et al*. [48] and is not presented here for brevity. The directional derivatives of W^{Ω} can be written as

$$\delta W^{\Omega} = \int_{\Omega}\int_{0}^{T} \mathbf{E}^2\, \delta\sigma\; dt\, d\Omega - \int_{\Omega}\int_{0}^{T} \overleftarrow{\mathbf{E}}\; \mathbf{E}^*\, \delta\sigma\; dt\;\; d\Omega. \tag{36}$$

ACKNOWLEDGMENT

The computations were performed on resources provided by the Swedish National Infrastructure for Computing (SNIC) at the HPC2N Center.

REFERENCES

[1] E. Denicke, G. Armbrecht, and I. Rolfes, "Radar distance measurements in circular waveguides involving intermodal dispersion effects," *Int. J. Microw. Wireless Technol.*, vol. 2, nos. 3–4, pp. 409–417, Aug. 2010.

[2] N. Pohl, T. Jaeschke, and K. Aufinger, "An ultra–wideband 80 GHz FMCW radar system using a SiGe bipolar transceiver chip stabilized by a fractional–N PLL synthesizer," *IEEE Trans. Microw. Theory Techn.*, vol. 60, no. 3, pp. 757–765, Mar. 2012.

[3] S. Ayhan, S. Scherr, A. Bhutani, M. Pauli, and T. Zwick, "Radar sensor for waveguide based distance measurements in machine tool components," in *Proc. IEEE MTT-S Int. Conf. Microw. Intell. Mobility (ICMIM)*, Apr. 2015, pp. 1–4.

[4] S. Ayhan, S. Scherr, P. Pahl, S. Walde, M. Pauli, and T. Zwick, "Radar–based high–accuracy angle measurement sensor operating in the K–band," *IEEE Sensors J.*, vol. 15, no. 2, pp. 937–945, Feb. 2015.

[5] B. Scheiner, F. Lurz, F. Michler, S. Linz, R. Weigel, and A. Koelpin, "Six–port based multitone and low–power radar system for waveguide measurements in smart factories," in *Proc. 48th Eur. Microw. Conf. (EuMC)*, Sep. 2018, pp. 1065–1068.

[6] U. Rosenberg *et al.*, "Bundled waveguide solution for multibeam satellite applications," in *Proc. 47th Eur. Microw. Conf. (EuMC)*, Oct. 2017, pp. 516–519.

[7] A. R. Dion and L. J. Ricardi, "A variable-coverage satellite antenna system," *Proc. IEEE*, vol. 59, no. 2, pp. 252–262, Feb. 1971.

[8] W. W. Wu, "Internet satellite challenges," in *Proc. 2nd Int. Conf. Evolving Internet*, Sep. 2010, pp. 31–35.

[9] T. Lee, "Global Internet access from space for Humanitarian applications," in *Proc. IEEE Int. Freq. Control Symp. (IFCS)*, May 2016, pp. 1–3.

[10] A. Isapour and A. Kouki, "Vertical LTCC integrated rectangular waveguide and transitions for millimeter–wave applications," *IEEE Trans. Microw. Theory Techn.*, vol. 67, no. 3, pp. 868–882, Mar. 2019.

[11] H. Lee, M. Uhm, S. Yun, and I. Yom, "Full-band transition from substrate integrated waveguide to rectangular waveguide," *Electron. Lett.*, vol. 51, no. 14, pp. 1089–1090, Jul. 2015.

[12] Y. Zhang, S. Shi, R. D. Martin, and D. W. Prather, "Broadband SIW-to-waveguide transition in multilayer LCP substrates at W-band," *IEEE Microw. Wireless Compon. Lett.*, vol. 27, no. 3, pp. 224–226, Mar. 2017.

[13] J. Li, L. Li, Y. Qiao, J. Chen, J. Chen, and A. Zhang, "Full Ka band waveguide-to-microstrip inline transition design," *J. Infr. Millim. THz. Waves*, vol. 39, no. 8, pp. 714–722, Aug. 2018.

[14] J. Pérez-Escudero, A. Torres-García, R. Gonzalo, and I. Ederra, "A simplified design inline microstrip-to-waveguide transition," *Electronics*, vol. 7, no. 10, p. 215, Sep. 2018.

[15] B. Y. El Khatib, T. Djerafi, and K. Wu, "Substrate-integrated waveguide vertical interconnects for 3-D integrated circuits," *IEEE Trans. Compon., Packag., Manuf. Technol.*, vol. 2, no. 9, pp. 1526–1535, Sep. 2012.

[16] B. Scheiner *et al.*, "Microstrip-to-waveguide transition in planar form using a substrate integrated waveguide," in *Proc. IEEE Radio Wireless Symp. (RWS)*, Jan. 2018, pp. 18–20.

[17] Q. Zhang and Y. Lu, "E-band 'T' shape transitions between substrate integrated waveguide and standard waveguide," in *Proc. Asia–Pacific Microw. Conf.*, Dec. 2008, pp. 1–4.

[18] O. Akgun and O. A. Tretyakov, "Solution to the Klein–Gordon equation for the study of time-domain waveguide fields and accompanying energetic processes," *IET Microw., Antennas Propag.*, vol. 9, no. 12, pp. 1337–1344, Sep. 2015.

[19] O. A. Tretyakov and O. Akgun, "Derivation of Klein-Gordon equation from Maxwell's equations and study of relativistic time-domain waveguide modes," *Prog. Electromagn. Res.*, vol. 105, pp. 171–191, 2010.

[20] Z. Lou and J.-M. Jin, "An accurate waveguide port boundary condition for the time-domain finite-element method," *IEEE Trans. Microw. Theory Techn.*, vol. 53, no. 9, pp. 3014–3023, Sep. 2005.

[21] F. Alimenti, P. Mezzanotte, L. Roselli, and R. Sorrentino, "A revised formulation of modal absorbing and matched modal source boundary conditions for the efficient FDTD analysis of waveguide structures," *IEEE Trans. Microw. Theory Techn.*, vol. 48, no. 1, pp. 50–59, Jan. 2000.

[22] S. Dvorak, "Exact, closed-form expressions for transient fields in homogeneously filled waveguides," *IEEE Trans. Microw. Theory Techn.*, vol. 42, no. 11, pp. 2164–2170, Nov. 1994.

[23] F. Moglie, T. Rozzi, P. Marcozzi, and A. Schiavoni, "A new termination condition for the application of FDTD techniques to discontinuity problems in close homogeneous waveguide," *IEEE Microw. Guid. Wave Lett.*, vol. 2, no. 12, pp. 475–477, Dec. 1992.

[24] T. Flisgen, H.-W. Glock, and U. VanRienen, "Compact time–domain models of complex RF structures based on the real eigenmodes of segments," *IEEE Trans. Microw. Theory Techn.*, vol. 61, no. 6, pp. 2282–2294, Jun. 2013.

[25] T. Flisgen, J. Heller, and U. VanRienen, "Time–domain absorbing boundary terminations for waveguide ports based on state–space models," *IEEE Trans. Magn.*, vol. 50, no. 2, pp. 145–148, Feb. 2014.

[26] G. Chen, L. Zhao, W. Yu, S. Yan, K. Zhang, and J.-M. Jin, "A general scheme for the discontinuous Galerkin time–domain modeling and S–parameter extraction of inhomogeneous waveports," *IEEE Trans. Microw. Theory Techn.*, vol. 66, no. 4, pp. 1701–1712, Apr. 2018.

[27] N. Aage, E. Andreassen, B. S. Lazarov, and O. Sigmund, "Giga-Voxel computational morphogenesis for structural design," *Nature*, vol. 550, no. 7674, pp. 84–86, Oct. 2017.

[28] J. D. Deaton and R. V. Grandhi, "A survey of structural and multidisciplinary continuum topology optimization: Post 2000," *Struct. Multidisciplinary Optim.*, vol. 49, no. 1, pp. 1–38, Jan. 2014.

[29] M. P. Bendsøe and O. Sigmund, *Topology Optimization: Theory, Methods, and Applications*. Berlin, Germany: Springer, 2003.

[30] K. Nomura, S. Yamasaki, K. Yaji, H. Bo, A. Takahashi, T. Kojima, and K. Fujita, "Topology optimization of conductors in electrical circuit," *Struct. Multidisciplinary Optim.*, vol. 59, no. 6, pp. 2205–2225, Jun. 2019.

[31] J. Wang, X.-S. Yang, X. Ding, and B.-Z. Wang, "Antenna radiation characteristics optimization by a hybrid topological method," *IEEE Trans. Antennas Propag.*, vol. 65, no. 6, pp. 2843–2854, Jun. 2017.

[32] N. Aage and V. Egede Johansen, "Topology optimization of microwave waveguide filters," *Int. J. Numer. Methods Eng.*, vol. 112, no. 3, pp. 283–300, Oct. 2017.
[33] E. Hassan, E. Wadbro, and M. Berggren, "Topology optimization of metallic antennas," *IEEE Trans. Antennas Propag.*, vol. 62, no. 5, pp. 2488–2500, May 2014.
[34] E. Hassan, E. Wadbro, L. Hägg, and M. Berggren, "Topology optimization of compact wideband coaxial-to-waveguide transitions with minimum-size control," *Struct. Multidisciplinary Optim.*, vol. 57, no. 4, pp. 1765–1777, Apr. 2018.
[35] E. Hassan, D. Noreland, E. Wadbro, and M. Berggren, "Topology optimisation of wideband coaxial-to-waveguide transitions," *Sci. Rep.*, vol. 7, no. 1, Apr. 2017, Art. no. 45110.
[36] E. Hassan, M. Berggren, B. Scheiner, F. Michler, R. Weigel, and F. Lurz, "Design of planar microstrip-to-waveguide transitions using topology optimization," in *Proc. IEEE Radio Wireless Symp. (RWS)*, Jan. 2019, pp. 1–3.
[37] F. X. Röhrl, J. Jakob, W. Bogner, D. Hageneder, and S. Zorn, "Differential wideband interconnects for organic millimeter wave chip packages: An effort to design an all-purpose RF chip package," in *Proc. 46th Eur. Microw. Conf. (EuMC)*, Oct. 2016, pp. 1465–1468.
[38] G. Kristensson, "Transient electromagnetic wave propagation in waveguides," *J. Electromagn. Waves*, vol. 9, nos. 5–6, pp. 645–671, 1995.
[39] D. Pozar, *Microwave Engineering*, 4th ed. Hoboken, NJ, USA: Wiley, 2012.
[40] T.-H. Loh and C. Mias, "Implementation of an exact modal absorbing boundary termination condition for the application of the finite–element time–domain technique to discontinuity problems in closed homogeneous waveguides," *IEEE Trans. Microw. Theory Techn.*, vol. 52, no. 3, pp. 882–888, Mar. 2004.
[41] M. Abramowitz and I. A. Stegun, *Handbook of Mathematical Functions With Formulas, Graphs, and Mathematical Tables*. Gaithersburg, MD, USA: National Bureau of Standards, 1964.
[42] E. Hassan, D. Noreland, R. Augustine, E. Wadbro, and M. Berggren, "Topology optimization of planar antennas for wideband near–field coupling," *IEEE Trans. Antennas Propag.*, vol. 63, no. 9, pp. 4208–4213, Sep. 2015.
[43] A. Taflove and S. Hagness, *Computational Electrodynamics: The Finite-Difference Time-Domain Method*, 3rd ed. Norwood, MA, USA: Artech House, 2005.
[44] E. Wadbro and M. Berggren, "Megapixel topology optimization on a graphics processing unit," *SIAM Rev.*, vol. 51, no. 4, pp. 707–721, Nov. 2009.
[45] E. Hassan, E. Wadbro, and M. Berggren, "Patch and ground plane design of microstrip antennas by material distribution topology optimization," *Prog. Electromagn. Res. B*, vol. 59, pp. 89–102, 2014.
[46] K. Svanberg, "A class of globally convergent optimization methods based on conservative convex separable approximations," *SIAM J. Optim.*, vol. 12, no. 2, pp. 555–573, Jan. 2002.
[47] N. Nikolova, Y. Li, Y. Li, and M. Bakr, "Sensitivity analysis of scattering parameters with electromagnetic time-domain simulators," *IEEE Trans. Microw. Theory Techn.*, vol. 54, no. 4, pp. 1598–1610, Jun. 2006.
[48] E. Hassan, E. Wadbro, and M. Berggren, "Time-domain sensitivity analysis for conductivity distribution in Maxwell's equations," Dept. Comput. Sci., Umeå Univ., Umeå, Sweden, Tech. Rep. UMINF 15.06, 2015.
[49] Z. Kordiboroujeni and J. Bornemann, "Designing the width of substrate integrated waveguide structures," *IEEE Microw. Wireless Compon. Lett.*, vol. 23, no. 10, pp. 518–520, Oct. 2013.
[50] O. Sigmund, "On the usefulness of non-gradient approaches in topology optimization," *Struct. Multidisciplinary Optim.*, vol. 43, no. 5, pp. 589–596, May 2011.
[51] Y. Zhang, S. Shi, R. D. Martin, and D. W. Prather, "Broadband SIW-to-waveguide transition in multilayer LCP substrates at W–band," *IEEE Microw. Wireless Compon. Lett.*, vol. 27, no. 3, pp. 224–226, Mar. 2017.
[52] X. Peng, J. Chen, H. Tang, D. Hou, P. Yan, and W. Hong, "Broadband and low-loss rectangular waveguide to substrate integrated waveguide transition with fin line," in *IEEE MTT-S Int. Microw. Symp. Dig.*, May 2015, pp. 1–3.
[53] G. Zhang, H. Yi, S. Wang, and M. Han, "Broadband right-angle transition from substrate integrated waveguide to rectangular waveguide," *Electron. Lett.*, vol. 53, no. 7, pp. 473–475, Mar. 2017.
[54] J. Dong, T. Yang, Z. Yang, and H. Peng, "Full Ka-band right-angle transition from substrate integrated waveguide to air-filled rectangular waveguide," *Electron. Lett.*, vol. 51, no. 22, pp. 1796–1798, Oct. 2015.
[55] T. Li and W. Dou, "Simple, compact and broadband right-angle transition between substrate integrated waveguide and rectangular waveguide at Ka-band," *Int. J. RF Microw. Comput.-Aided Eng.*, vol. 27, no. 4, 2017, Art. no. e21080.
[56] I. Mohamed and A. R. Sebak, "Broadband transition of substrate–integrated waveguide-to-air-filled rectangular waveguide," *IEEE Microw. Wireless Compon. Lett.*, vol. 28, no. 11, pp. 966–968, Nov. 2018.

Emadeldeen Hassan received the B.Sc. and M.Sc. degrees in electronics and communication engineering from Menoufia University, Menouf, Egypt, in 2001 and 2006, respectively, and the Licentiate and Ph.D. degrees in computational science and engineering from Umeå University, Umeå, Sweden, in 2013 and 2015, respectively.

From 2017 to 2018, he was a Post-Doctoral Fellow with the Department of Computing Science, Umeå University, Umeå, Sweden, where he is currently a Guest Researcher. In 2018, he was a Guest Scientist with the Institute for Electronics Engineering, Friedrich-Alexander University, Erlangen, Germany. Since 2016, he has been an Assistant Professor with the Department of Electronics and Electrical Communication Engineering, Menoufia University. His research interests include numerical methods in electromagnetics (EM), antenna design optimization, waveguides' transitions optimization, medical applications of EM, electromagnetic band gap structures (EBG), and defected ground structures, nondestructive evaluation and testing, optimization methods, and parallel programming.

Benedict Scheiner (S'17) received the B.S. degree in medical engineering and the M.S. degree in electrical engineering from the Friedrich-Alexander-Universitët Erlangen-Nürnberg (FAU), Erlangen, Germany, in 2014 and 2017, respectively, where he is currently pursuing the Ph.D. degree with the Institute for Electronics Engineering.

His main research topic is system design of different RF sensor systems mainly for industrial applications.

Mr. Scheiner received together with colleagues the first place award at the student design competition about radar system design at the IEEE International Microwave Symposium (IMS) in 2017, 2018, and 2019. He received the Graduate Student Challenge at the IMS 2018.

Fabian Michler (S'16) received the B.S. and M.S. degrees in electrical engineering and communications engineering from the Darmstadt University of Technology, Darmstadt, Germany, in 2013 and 2016, respectively.

In 2016, he joined the Institute for Electronics Engineering, Friedrich-Alexander-Universitët Erlangen-Nürnberg, Erlangen, Germany, as Research Assistant. His current research interests include RF front ends and microwave circuit design for precise low-power radar systems, particularly for the remote detection of human vital parameters and industrial metering.

Mr. Michler is a member of the IEEE Microwave Theory and Techniques Society (IEEE MTT-S). He was a recipient of the First Prize of the Low-Power Radar Student Design Competition of the IEEE International Microwave Symposium in 2017, 2018, and 2019.

Martin Berggren received the Ph.D. degree in computational and applied mathematics from Rice University, Houston, TX, USA, in 1996.

He is currently a Professor of scientific computing with Umeå University, Umeå, Sweden. He held a lectureship position at Uppsala University, Uppsala, Sweden, and research positions at the Swedish Defence Research Agency, Stockholm, Sweden, and Sandia National Laboratories, Albuquerque, NM, USA. His research interests concern numerical methods for partial differential equations and, in particular, computational design optimization for acoustic and electromagnetic wave propagation problems.

Eddie Wadbro received the M.Sc. degree in mathematics from Lund University, Lund, Sweden, in 2004, and the Licentiate and Ph.D. degrees in scientific computing from Uppsala University, Uppsala, Sweden, in 2006 and 2009, respectively.

Since 2009, he has been an Assistant Professor with the Department of Computing Science, Umeå University, Umeå, Sweden. His research interests concern mathematical modeling, development, and analysis of efficient numerical methods for differential equations, primarily within the fields of design optimization and inverse problems.

Franz Röhrl received the M.Sc. degree in electrical engineering and information technology from the Technical University of Munich, Munich, Germany, in 2013. He is currently pursuing the Ph.D. degree in PCB technology for millimeter-wave applications at Friedrich-Alexander-Universitët Erlangen-Nürnberg (FAU), Erlangen, Germany.

His main research interest is the design and optimization of high-frequency millimeter-wave submounts.

Stefan Zorn received the Dipl.Ing. degree in electronics engineering and the Dr. Ing. degree from the Friedrich-Alexander-Universitët Erlangen-Nürnberg, Erlangen, Germany, in 2007 and 2012, respectively.

Since 2012, he has been working as the Head of Research and Development PCB Technology, Rohde & Schwarz GmbH & Company, KG, Teisnach, Germany. He has been the Chair of RF engineering with the Deggendorf Institute of Technology, Deggendorf, Germany, since 2016. His research field has been the precise localization of mobile phones in natural disaster scenarios.

Robert Weigel (S'88–M'89–SM'95–F'02) was born in Ebermannstadt, Germany, in 1956. He received the Dr. Ing. and Dr. Ing.habil. degrees in electrical engineering and computer science from the Technical University of Munich, Munich, Germany, in 1989 and 1992, respectively.

From 1994 to 1995, he was a Guest Professor of SAW technology with the Vienna University of Technology, Vienna, Austria. He was a Research Engineer, a Senior Research Engineer, and a Professor of RF circuits and systems with the Technical University of Munich until 1996. From 1996 to 2002, he was the Director of the Institute for Communications and Information Engineering, University of Linz, Linz, Austria, where he co-founded the company DICE, Linz, in 1999, which split into an Infineon Technologies (DICE) and an Intel (DMCE) company, which are devoted to the design of radio-frequency integrated circuits (RFICs) and monolithic microwave integrated circuits (MMICs). In 2000, he was appointed as a Professor of RF engineering with Tongji University, Shanghai, China. Since 2002, he has been the Head of the Institute for Electronics Engineering, Friedrich-Alexander-Universitët Erlangen-Nürnberg, Erlangen, Germany, where he co-founded the companies eesy-id, Erlangen, and eesy-ic Nuremberg, Germany, in 2009 and 2012, respectively. He has authored or coauthored more than 900 articles. He has been engaged in research and development of microwave theory and techniques, electronic circuits and systems, and communication and sensing systems.

Dr. Weigel served in various roles for the IEEE Microwave Theory and Techniques Society (IEEE MTT-S) and the IEEE Ultrasonics, Ferroelectrics, and Frequency Control Society (UFFC-S). He has been the Founding Chair of the Austrian COM/MTT Joint Chapter, a Region 8 MTT-S Coordinator, a Distinguished Microwave Lecturer, the IEEE MTT-S AdCom Member, and the 2014 MTT-S President.

Fabian Lurz (S'13–M'20) received the B.Sc. and M.Sc. degrees in information and communication technology from the Friedrich-Alexander-Universitët Erlangen-Nürnberg (FAU), Erlangen, Germany, in 2010 and 2013, respectively.

In 2013, he joined the Institute for Electronics Engineering, FAU, as a Research Assistant, where he became the Group Leader of the Electronic Systems Group in 2017. His current research interests include microwave circuits and systems, especially for low-cost and low-power metrology applications.

Mr. Lurz was a recipient of the First Prize of the High Sensitivity Radar Student Design Competition of the IEEE International Microwave Symposium in 2014, 2017, and 2018 and the IEEE Microwave Theory and Techniques Society Graduate Fellowship Award in 2016.